



# Preparation of Fe–As alloys by mechanical alloying and vacuum hot-pressed sintering: microstructure evolution, mechanical properties, and mechanisms

Fei Chai, Fei-Ping Zhao\*, Zhan Hu, Shi-Yi Wen, Ben-Hammouda Samia, Ze-Lin Fu, Xin-Ting Lai, Yan-Jie Liang\*, Xiao-Bo Min, Li-Yuan Chai

Received: 23 October 2023 / Revised: 16 December 2023 / Accepted: 17 December 2023 / Published online: 14 June 2024  
© Youke Publishing Co., Ltd. 2024

**Abstract** Arsenic materials have attracted great attention due to their unique properties. However, research concerning iron–arsenic (Fe–As) alloys is very scarce due to the volatility of As at low temperature and the high melting point of Fe. Herein, a new Fe–As alloy was obtained by mechanical alloying (MA) followed by vacuum hot-pressed sintering (VHPS). Moreover, a systematic study was carried out on the microstructural evolution, phase composition, leaching toxicity of As, and physical and mechanical properties of Fe–As alloys with varying weight fractions of As (20%, 25%, 30%, 35%, 45%, 55%, 65%, and 75%). The results showed that pre-alloyed metallic powders (PAMPs) have a fine grain size and specific super-

saturated solid solution after MA, which could effectively improve the mechanical properties of Fe–As alloys by VHPS. A high density ( $> 7.350 \text{ g}\cdot\text{cm}^{-3}$ ), low toxicity, and excellent mechanical properties could be obtained for Fe–As alloys sintered via VHPS by adding an appropriate amount of As, which is more valuable than commercial Fe–As products. The Fe-25% As alloy with low toxicity and a relatively high density ( $7.635 \text{ g}\cdot\text{cm}^{-3}$ ) provides an ultra-high compressive strength (1989.19 MPa), while the Fe-65% As alloy owns the maximum Vickers hardness ( $\text{HV}_{0.5} 899.41$ ). After leaching by the toxicity characteristic leaching procedure (TCLP), these alloys could still maintain good mechanical performance, and the strengthening mechanisms of Fe–As alloys before and after leaching were clarified. Changes in the grain size, microstructure, and phase distribution induced significant differences in the compressive strength and hardness.

**Supplementary Information** The online version contains supplementary material available at <https://doi.org/10.1007/s12598-024-02733-6>.

F. Chai, F.-P. Zhao\*, Z. Hu, S.-Y. Wen, Z.-L. Fu, X.-T. Lai, Y.-J. Liang\*, X.-B. Min, L.-Y. Chai  
School of Metallurgy and Environment, Central South University, Changsha 410083, China  
e-mail: feiping.zhao@csu.edu.cn

Y.-J. Liang  
e-mail: liangyanjie1982@163.com

F.-P. Zhao, Z. Hu, Y.-J. Liang, X.-B. Min, L.-Y. Chai  
Chinese National Engineering Research Center for Control & Treatment of Heavy Metal Pollution, Institute of Environmental Engineering, Central South University, Changsha 410083, Hunan, China

S.-Y. Wen  
State Key Laboratory of Powder Metallurgy, Central South University, Changsha 410083, China

B.-H. Samia  
Department of Building, Civil, and Environmental Engineering, Concordia University, Montreal H3G 1M8, Canada

**Keywords** Mechanical alloying; Vacuum hot-pressed sintering; High-pressure; Arsenic–iron alloys; Mechanical properties

## 1 Introduction

Arsenic (As) is a ubiquitous metalloid of concern at many mine sites and is a residual harmful element in mine waste because of its high toxicity [1]. For example, high concentrations of arsenic weaken grain boundary cohesion and cause the embrittlement of steel due to microsegregation and grain boundary segregation, which further deteriorates the thermal processing and mechanical properties of steel [2]. Therefore, many strategies have been applied to control and eliminate the concentration of As during metallurgical



processes [3–5]. These methods can significantly decrease the As concentration in these wastes, but there is still a risk of secondary pollution [3]. Moreover, this process is critical for its high carbon emissions and compatibilization during production, and these treatments cannot produce valuable As products, resulting in a significant waste of As resources [6, 7]. Therefore, it is necessary to develop an eco-friendly strategy for As resource utilization.

As is a dangerous pollutant but a vital resource for developing a new arsenic material. In recent years, arsenic materials have attracted wide attention due to their unique electronic conductivity [8, 9], thermal conductivity [10–12], and magnetic properties [13–15]. For instance, Tian et al. [12] discovered super-high thermal conductivity in cubic boron arsenide (BAs) crystals, which is now the only known semiconductor with a band gap comparable to that of silicon. Song et al. [16, 17] successfully synthesized highly oriented black arsenic–phosphorus (b-AsP) by precise control over the vapor transport process, and the antioxidation property of highly oriented b-AsP increased. Moreover, gallium arsenide (GaAs) [18, 19] and iron arsenide (FeAs)-based superconductors [20, 21] as well as indium arsenide (InAs) semiconductors [22, 23] have also raised increasing concern; however, there are few studies on iron–arsenic (Fe–As) alloys [24], especially on their synthesis, which is important for understanding and developing the iron arsenide (FeAs)-based materials. This could be due to the volatility of As at low temperature and the high melting point of Fe. Additionally, at present, commercial Fe–As products are popularly known as arsenic matte and are of great interest for counterweight material application due to their excellent economic value, large yield, and high proportion ( $\sim 7.3 \text{ g}\cdot\text{cm}^{-3}$ ). However, the leaching toxicity of the arsenic matte is sometimes beyond the permitted scope and thus contains security risks [25]. Furthermore, the relationships among the microstructure, phase composition, and mechanical properties of the Fe–As products were ambiguous. Therefore, the conversion of hazardous materials containing arsenic into useful products and the quantitative investigation of the related connections are highly important not only for environmental protection but also for As resource utilization.

Recently, various techniques, including self-propagating high-temperature synthesis (SHS), spark plasma sintering (SPS), mechanical alloying (MA), vacuum hot-pressed sintering (VHPS), vacuum induction melting (VIM), and casting mechanically activated combustion, have been developed to prepare various alloys and reduce environmental pollution [26–33]. Among those techniques, VHPS is a lower-cost, more stable, easy-to-control powder consolidation technology [34]. During hot-pressed sintering, vacuuming can not only prevent the material from being oxidized but also promote the elimination of gases

produced during the sintering process and the densification process. In addition, this method involves a relatively low sintering temperature and grain growth inhibition, which easily results in a fine grain structure and good mechanical properties. Therefore, the VHPS method was applied in this study. However, iron (Fe), which has a high self-diffusion activation enthalpy ( $280 \text{ kJ}\cdot\text{mol}^{-1}$ ), is a refractory metal [35]; therefore, a high diffusion activation energy is needed for sintering at low temperature. Mechanical alloying (MA) by decreasing crystallite sizes (the reduction in the diffusion distance) and increasing some metallurgical defects, such as vacancies, dislocations, and grain boundaries, could reduce the diffusion activation energy [36], which would be promising in solving diffusion bottlenecks. High-energy mechanical milling is a well-accepted approach for fabricating pre-alloyed metallic powders (PAMPs) and nanocrystalline metal powders because it is cost-effective, simple, and applicable to most kinds of materials [37]. Moreover, the metal elements in the PAMPs undergo alloying, which leads to high alloying that can be achieved with decreased activation energy and temperature during the sintering process. Importantly, PAMPs have a specific super-saturated solid solution, which can effectively enhance their hardness and strength. Therefore, the MA method combined with VHPS can result in an almost full density and good mechanical properties for the resulting alloys.

Based on these considerations, the purpose of this paper is to develop a new Fe–As alloy by an MA with the subsequent VHPS method and to quantitatively reveal the relationships among the microstructure, phase compositions, and mechanical properties of Fe–As alloys. Therefore, in this work, a series of Fe–As alloys with varying weight fractions of As (20%, 25%, 30%, 35%, 45%, 55%, 65%, and 75%) were prepared, and the effects of As addition on the surface morphologies, phase compositions, physical density, leaching toxicity, the mechanical properties, and corresponding mechanisms were studied in depth.

## 2 Experimental

### 2.1 Sample preparation

Commercially available Fe powders (99.5%) and As blocks (99.5%) were purchased from Shanghai Aladdin Industrial Corporation, China. The Fe powders were sieved through 300-mesh sieves for subsequent analyses and experiments. The As blocks were MA to obtain As powders in a high-energy planetary ball mill (IKAYXQM-4, Changsha Miqu Instrument Equipment Co., Ltd.) under the following milling parameters:  $320 \text{ r}\cdot\text{min}^{-1}$ , 1 h, zirconium dioxide balls

(20 mm in diameter) and tank (500 ml), and a ball-to-powder weight ratio of 20:1.

Bulk nanostructure Fe–As alloys were synthesized by using MA followed by VHPS, as seen in Fig. 1a. In detail, first, the different weight fractions of As powders (20%, 25%, 30%, 35%, 40%, 45%, 55%, 65% and 75%) with the Fe powders were weighed in a glove box with high-purity argon to minimize oxidation pollution and then mechanically alloyed in a high-energy planetary ball mill using zirconia spheres (10 and 5 mm in diameter, the ratio is 1:1) under an argon atmosphere for 40 h. The weighted rate of the milling spheres and the mixed powder was 20:1, and the rotation speed was  $320 \text{ r}\cdot\text{min}^{-1}$ . Pre-alloyed metallic powders (PAMPs) were obtained.

Second, 4 g PAMPs was weighed and loaded into a graphite mold in the glove box, then heated to  $400 \text{ }^\circ\text{C}$  in a vacuum hot-pressed furnace (OTF-1200X-VHP4, Hefei Kejing Material Technology Co., Ltd.) with a pressure of 30 MPa and held for 0.5 h ( $10 \text{ }^\circ\text{C}\cdot\text{min}^{-1}$ ) to obtain preliminary densification and avoid excessive crystal grain growth. Then, further consolidation sintering was conducted at a high temperature of  $800 \text{ }^\circ\text{C}$ , and a constant pressure of 30 MPa for 1 h was used to reduce the porosities.

Finally, the samples were cooled naturally in the furnace, resulting in high-density bulk Fe–As alloys with a cylindrical piece of  $\Phi 12.70 \text{ mm} \times 4.12 \text{ mm}$ . The obtained Fe–As alloys were named Fe-20% As, Fe-25% As, Fe-30% As, Fe-35% As, Fe-40% As, Fe-45% As, Fe-55% As, Fe-65% As, and Fe-75% As, according to the weight fractions

of As in the starting materials. A high-vacuum environment ( $< 1 \times 10^{-3} \text{ Pa}$ ) was maintained during the process to avoid oxidation.

## 2.2 Leaching tests

The stability of As in the sintered specimens was determined according to the toxicity characteristic leaching procedure (TCLP). The Fe–As alloy was extracted with  $0.1\text{-mol}\cdot\text{L}^{-1}$  acetate at a liquid-to-solid (L/S) ratio of 20 and horizontally vibrated for 18 h at room temperature. After extraction and filtration of leachates, the concentrations of As and Fe were analyzed via inductively coupled plasma emission spectrometry (ICP-OES, PerkinElmer, Germany).

A Chinese regulatory method (HJ/T299-2007) was used to evaluate the leachability of the specimens under acid rain exposure. The sulfuric acid and nitric acid method simulated acid rain using sulfuric and nitric acids with a mass ratio of 2:1 at pH 3.20. The samples were placed in an L/S ratio of 10 and horizontally vibrated for 18 h at room temperature.

## 2.3 Materials characterizations

The morphologies and microstructures of the original Fe and As powders, the PAMPs produced by MA, and the sintered Fe–As alloys produced by VHPS before and after leaching were analyzed by scanning electron microscope (SEM, Zeiss Sigma 300, Germany) with energy-dispersive X-ray

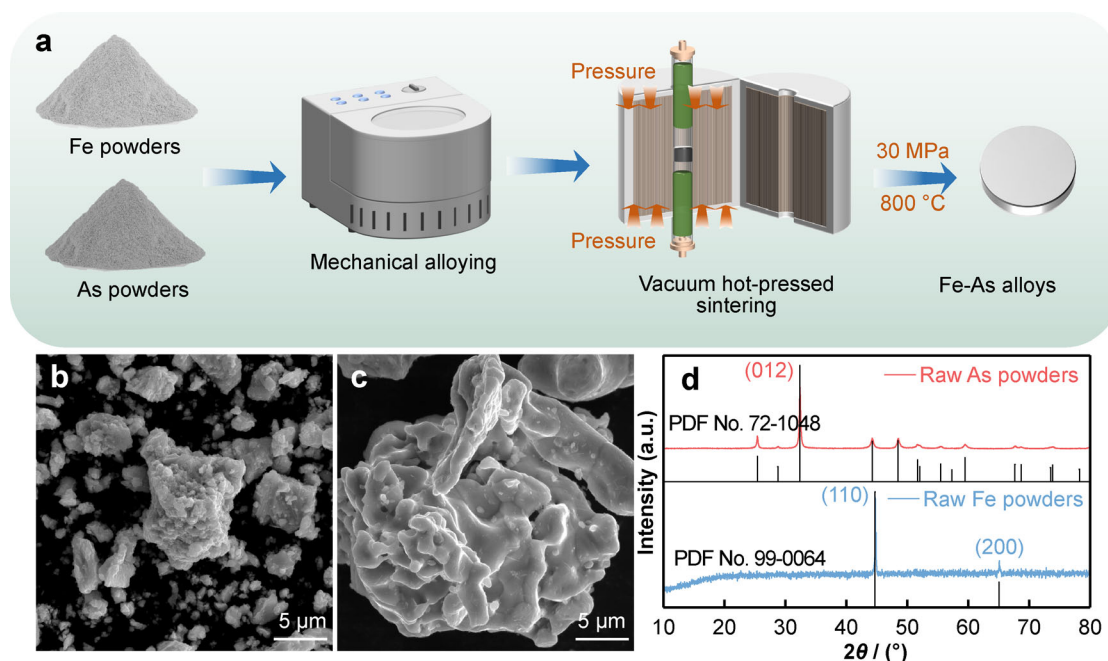


**Fig. 1** a Schematic illustration of synthesis of Fe–As alloys; SEM images of raw materials: b As powders, c Fe powders, and d corresponding XRD patterns

spectrometry (EDS). The phase compositions and crystal structures of the samples were verified using a Bruker D8 Advance X-ray diffractometer (XRD) and X-ray photoelectron spectroscopy (XPS, XP-300 Analyzer, USA). The transmission electron microscope (TEM) samples were prepared from VHPS samples using a FEI Scios Dual-Beam/scanning electron microscope (FIB/SEM) system with a standard FIB lift-out method. The obtained thinning specimen was attached to a copper grid used for characterization in detail. The lamellae specimen was observed by utilizing a field emission transmission electron microscope (TEM, JEM-F200, Japan). The actual density and apparent porosities of Fe–As alloys were measured by the Archimedes method in triplicate after removing the surface impurities. For electron back-scatter diffraction (EBSD) measurements, the specimens were first ground by 400-, 800-, 1200-, 1500-, and 2000-grit silicon carbide (SiC) abrasive papers and then polished in an argon ion beam. The samples were analyzed on the HELIOS Nanolab G4 PFIB equipped with an Oxford Instruments Nordlys max3 EBSD. The scans were performed using a step size of 0.6  $\mu\text{m}$ . EBSD data were handled by Channel 5 software used to produce inverse pole figure (IPF) measurements, with high-angle grain boundaries (HAGBs,  $> 15$  misorientation) indicated as black lines and low-angle grain boundaries (LAGBs,  $> 2$  misorientation) indicated by red lines.

Compression tests were conducted according to GB/T 7314–2017 “Sintered Metallic Materials—Compression test method at room temperature. Briefly, the compressive strength of alloys was tested by INSTRON 1342 at a speed of 0.3 mm·min<sup>-1</sup>. Before the compression test, the upper and lower surfaces of the sintered samples were polished with 1000-grit emery paper. Each test was conducted in triplicate. Vickers microhardness test was used to determine the hardness of various metals. The hardness of the alloys was measured by a Vickers hardness tester (Falcon 507, Innovatest Corp). For each sample, six indents were carried out using an average load of 500 g and a dwell time of 10 s. To ensure that the hardness result of each indent was not affected by others, the distance between the test points was 1 mm. The compressive strength and Vickers hardness of the sintered alloys after the leaching test by TCLP were also measured.

### 3 Results and discussion

#### 3.1 Characterization of mechanically alloyed powders

Figure 1b–d shows SEM images and XRD diffraction patterns of raw As and Fe powders, respectively. It can be seen in Fig. 1b that there are many small particles loosely

covering the surface of large particles and the raw As powders are irregular shapes with different sizes. In addition, XRD results of the As powders are shown in Fig. 1d. The raw As powders exhibited clear diffraction peaks, which was consistent with what was observed for As (PDF No. 72-1048). However, the Fe powder particles present a spiral void shape on their surface, and there are a few spherical particles (Fig. 1c). A sharper characteristic peak (110) corresponding to the Fe phase is observed, indicating that the Fe phase is the  $\alpha$ -Fe phase (Fig. 1d).

Figure 2 presents the micromorphology of the PAMPs with varying As contents. When the content of As addition was low (20%–35% As), as shown in Fig. 2a–d, the powder particles had an irregular spherical shape, and there was no remarkable change in the micromorphology of the powders and a small amount of As particles on the surface of Fe particles. However, a significant difference in the surface morphology and shape of the powder can be seen when As was further added, as shown in Fig. 2e–i. The powders were finer and more uniform with As addition, and the average size of the powders decreased gradually to less than 5  $\mu\text{m}$ . It is more likely that irregular As powder particles are more conducive to destroying the surface of the Fe substrate during the mechanical activation process of ball milling, shortening the distance between the two phases, lowering the activation energy, increasing bonding, and achieving PAMPs by entering the Fe lattice [29, 38]. This provides a good foundation for the subsequent hot-pressed sintering process to prepare denser and better mechanical properties of Fe–As alloys. The mapping results of PAMPs with varying As contents are shown in Table S1. According to the results, it was found that the actual compositions of the powders after MA were very close to the design compositions.

XRD analyses were carried out to further confirm the phase composition of PAMPs. As shown in Fig. 3a, it can be noted that there are no raw As peaks in the PAMPs except for the Fe-75% As, indicating that As was dissolved in Fe and formed a solid solution phase or reacted into an intermediate compound during the MA process. There was only a significant  $\alpha$ -Fe phase with the diffraction peak (110) and a characteristic peak of the FeAs phase with low intensity when a low amount of As (20%–55% As) was added, suggesting that a number of solid solution phases ( $\alpha$ -Fe[As]) were formed. Furthermore, according to the enlarged view (Fig. 3b), the position of the  $\alpha$ -Fe characteristic peak shifted to a higher angle than that of XRD result for the raw Fe powder, and the intensity of the FeAs characteristic peak increased when the weight fraction of As ranged from 20 to 55%. This confirmed that a lot of solid solution phases ( $\alpha$ -Fe[As]) and intermediate compounds (FeAs) were formed. The FeAs intermetallic phase



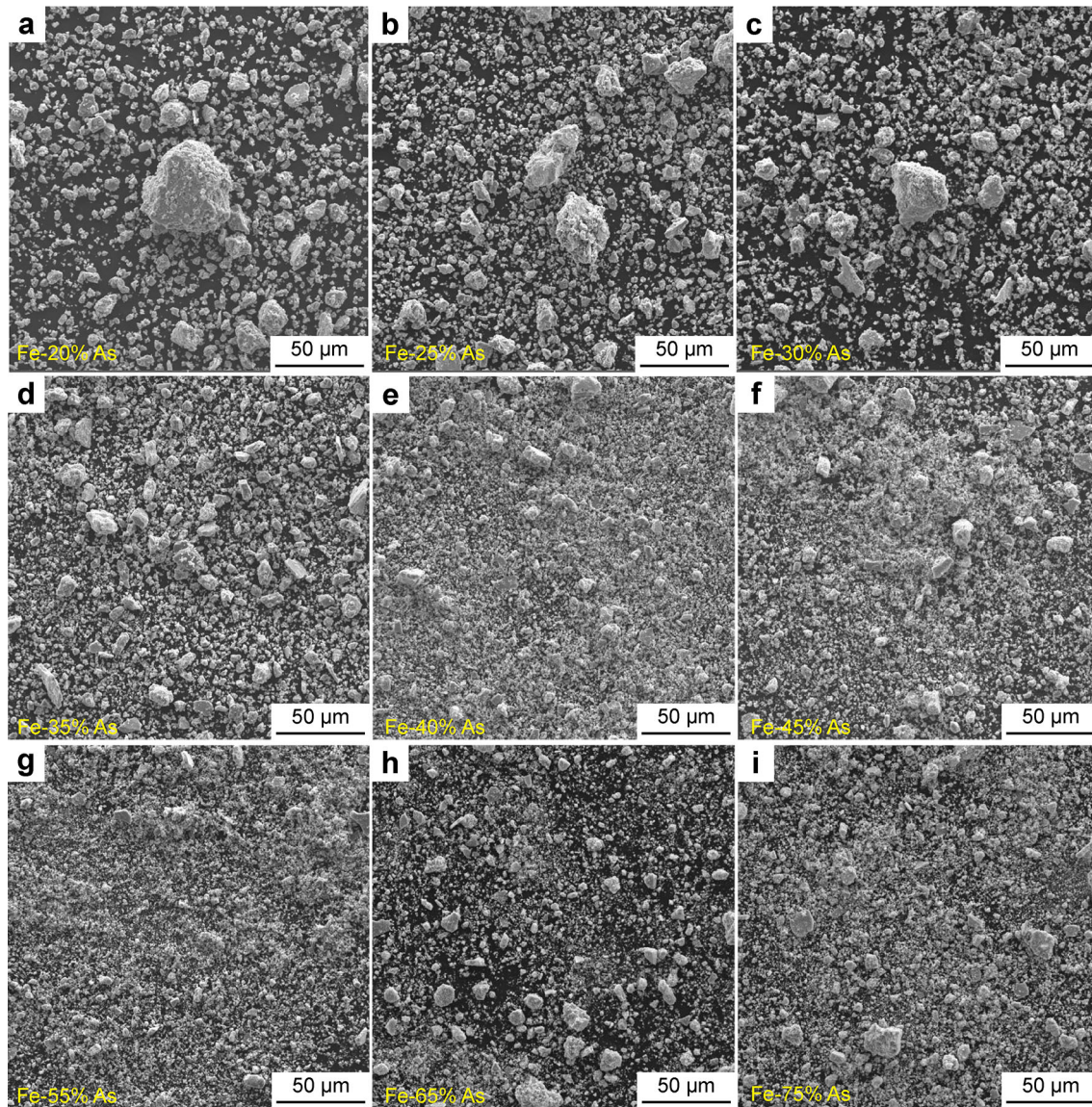


**Fig. 2** SEM images of PAMPs: **a** Fe-20% As, **b** Fe-25% As, **c** Fe-30% As, **d** Fe-35% As, **e** Fe-40% As, **f** Fe-45% As, **g** Fe-55% As, **h** Fe-65% As, and **i** Fe-75% As

was transformed to the  $\text{FeAs}_2$  phase, and the raw As characteristic peak was detected in the PAMPs of Fe-75% As due to the excessive As addition.

The quantitative XRD analysis results were obtained (Table 1). The crystallite size, dislocation density, and microstrain could be calculated from the Scherrer equation [39, 40]:

$$D = \frac{K\lambda}{\beta \cos\theta} \quad (1)$$

where  $D$  (nm) is the crystallite size,  $\lambda$  is the wavelength of Cu  $K\alpha$  radiation (0.154 nm),  $K$  is a constant (0.9), and  $\theta_B$  represents the Bragg angle. The true XRD peak broadening  $B$  (FWHM) of the Fe–As powders was obtained after eliminating the instrumental contribution.

$\delta$  ( $\text{nm}^{-2}$ ) and  $\varepsilon$  are the dislocation density and the microstrain, respectively, which could be calculated by the equation:

$$\delta = \frac{1}{D^2} \quad (2)$$

$$\varepsilon = \frac{B}{4\tan\theta_B} \quad (3)$$

According to the result, it is well-known that during the MA process, a high dislocation density is generated, which increases the microstrain, leading to the broadening of the XRD peaks. Meanwhile, the significant refinement of crystallite size with an increase in the lattice microstrain implies a large amount of defect density (e.g., dislocation)

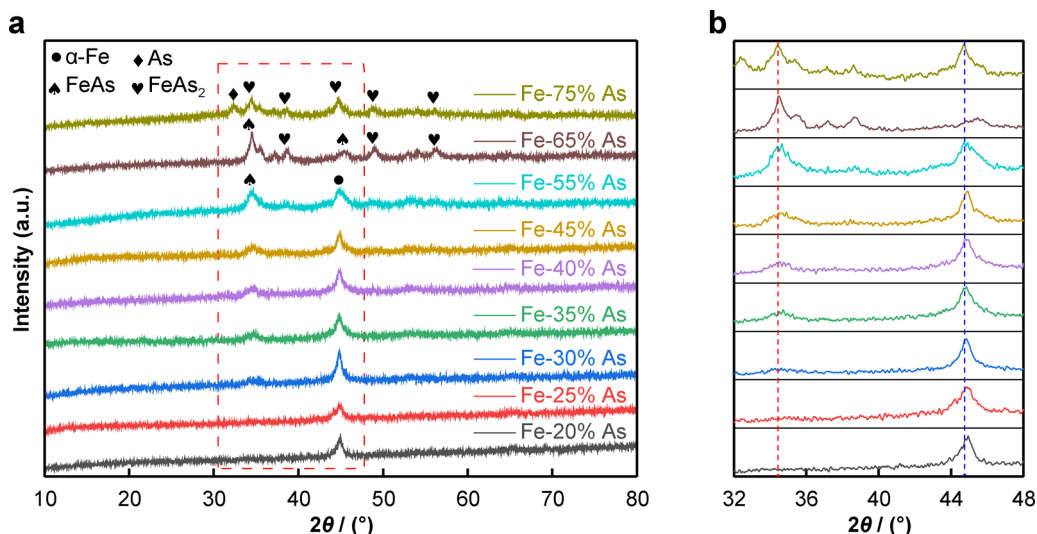


**Fig. 3** **a** XRD patterns of PAMPs with varying As contents and **b** enlarged view and (inset) red line representing position of FeAs<sub>2</sub> phase and blue line representing position of  $\alpha$ -Fe phase

**Table 1** Results of XRD analyses of PAMPs by MA

Sample	Crystallite size (nm)	Dislocation density ( $10^{15} \text{ m}^{-2}$ )	Strain ( $10^{-3}$ )
Fe-20% As	12.57	11.95	9.07
Fe-25% As	13.83	13.17	9.20
Fe-30% As	11.89	16.53	10.39
Fe-35% As	9.98	24.77	12.63
Fe-40% As	9.96	25.85	12.83
Fe-45% As	7.20	25.41	16.38
Fe-55% As	6.66	22.58	15.60
Fe-65% As	11.85	9.37	8.49
Fe-75% As	9.07	13.12	11.93

inside PAMPs [41]. Based on the above analyses, it could be concluded that a fine pre-alloyed Fe–As powder could be obtained by the MA method, which has a specific super-saturated solid solution after MA.

## 3.2 VHPS alloy characterizations

### 3.2.1 Microstructure and phase compositions

The microstructures of the Fe–As alloys sintered by VHPS with different As contents are presented in Fig. 4. From the images of the VHPS alloys, one can notice that there were a few large and many small voids because of difficult densification and poor bonding when a small amount of As was added. However, there are tiny amounts of microvoids on the surface of Fe–As alloys with As addition, indicating that fully dense microstructures are achieved by the VHPS combined with the MA method. In addition, these alloys exhibit a homogeneous

microstructure without apparent aggregation except for the Fe-75% As alloy. The decrease in voids and homogeneous microstructure could be attributed to the profound effect of As addition and the significant VHPS method, which promote the elimination of gases produced during the sintering process and the densification process [35]. Additionally, the PAMPs with a fine size and the formation of a super-saturated solid solution and intermediate compound could contribute to the reduction of voids [13]. However, it was found that the microstructure of the sintered Fe-75% As sample, which had several voids and a connected network structure, was obviously different from that of the other sintered samples. This may be due to the presence of the amount of raw As resulting from the excessive increase in the weight fraction of As, which decreased the spacing between As particles, increasing the susceptibility of the sample to oxidation [42]. Thus, the particles easily aggregated and grew through atomic diffusion in the VHPS process.



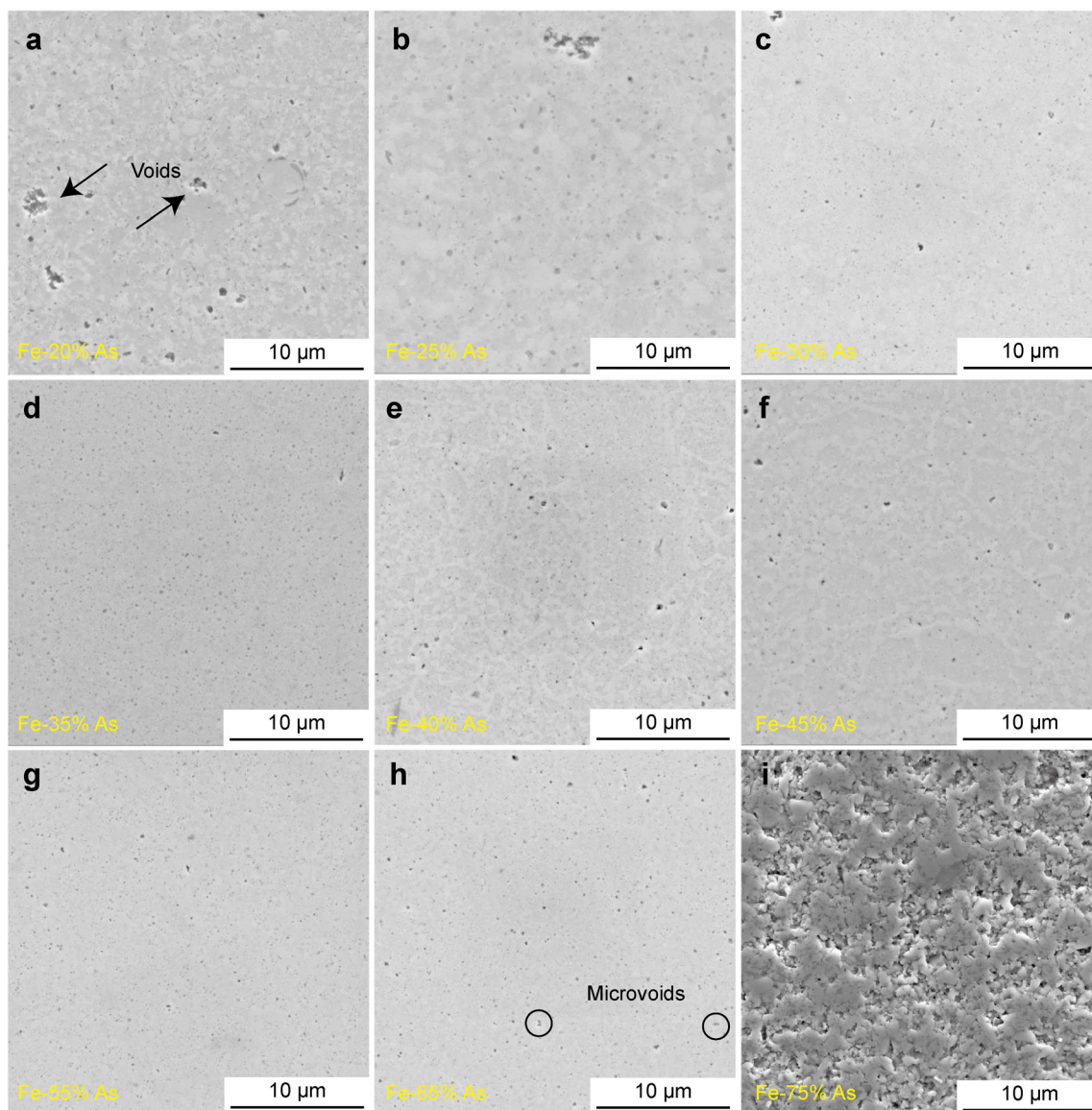


**Fig. 4** SEM micrographs of Fe–As alloys sintered by VHPS: **a** Fe-20% As, **b** Fe-25% As, **c** Fe-30% As, **d** Fe-35% As, **e** Fe-40% As, **f** Fe-45% As, **g** Fe-55% As, **h** Fe-65% As, and **i** Fe-75% As

To confirm the details of the microstructure and phase distribution of the Fe–As alloys sintered by VHPS, back-scattered electron (BSE) and mapping images of the as-sintered Fe–As alloys are also shown in Fig. 5. The corresponding EDS results are shown in Tables S2 and S3. As shown in Fig. 5a–d, the composites consist of two types of phases: gray–white and gray areas. Combined with the EDS results (Table S3), the gray–white and gray areas corresponded to the  $\text{Fe}_2\text{As}$  and  $\alpha\text{-Fe}$  phases. In addition, respectively, the gray–white areas increase, while the gray areas decrease with As addition. For Fig. 5e–g, it can be concluded that the gray areas are the  $\text{Fe}_2\text{As}$  phases and the gray–white areas are the FeAs phases, and finally, the microstructure of Fe-55% As

consists of only a uniform gray–white phase with further As addition. When the weight fraction of As was excessive, the areas became dark gray, and the dominant phases were completely the  $\text{FeAs}_2$  phases according to EDS results. According to the BSE mapping results (Fig. 5, Table S2), it was found that the actual compositions of alloys obtained by VHPS were very close to the design compositions and the distribution of As gradually became uniform as the As content's appropriate addition. However, it is worth noting that As and Fe aggregated, and the atomic ratio (at%) of oxygen (O) reached 8.34 in Fe-75% As (Fig. 5i) due to the excessive addition of As, resulting in surface oxidation and different microstructures compared with other alloys.

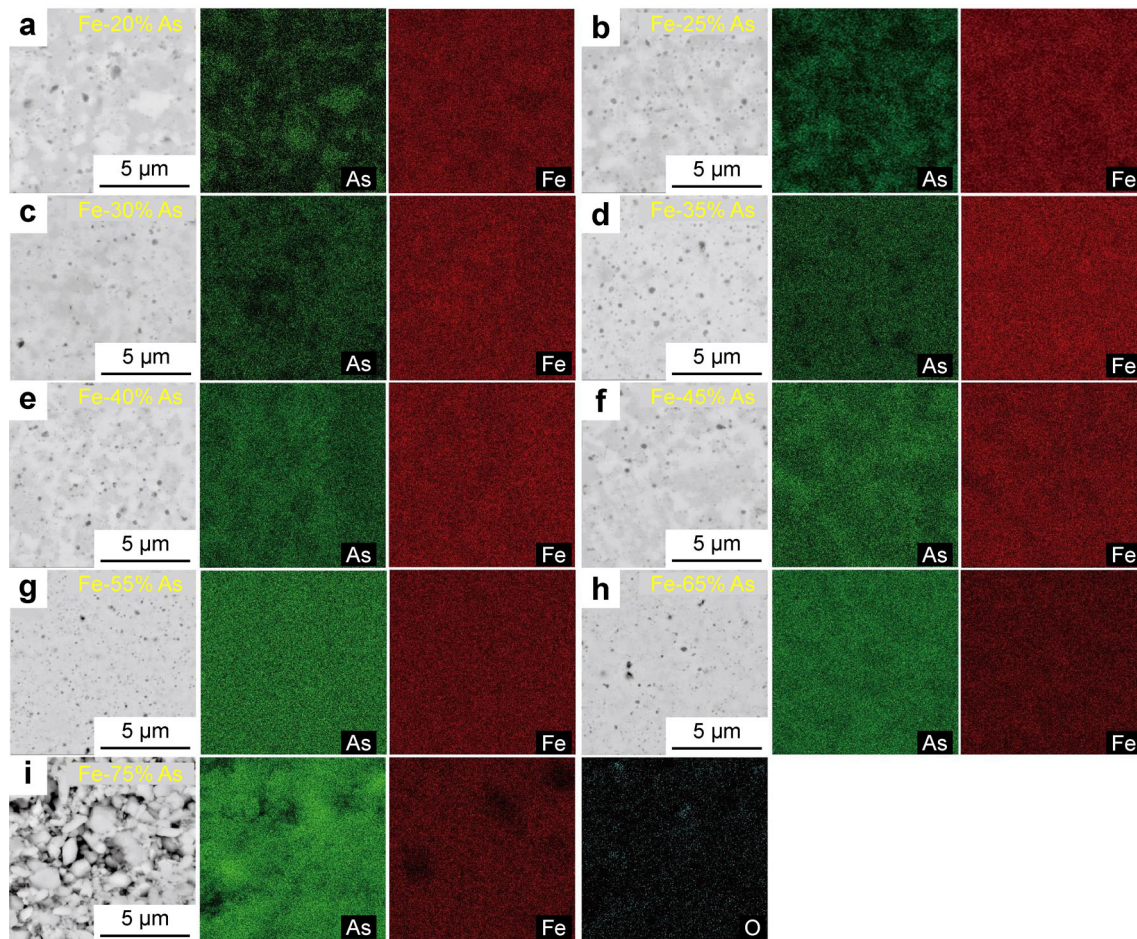


**Fig. 5** BSE and mapping micrographs of Fe–As alloys sintered by VHPS: **a** Fe-20% As, **b** Fe-25% As, **c** Fe-30% As, **d** Fe-35% As, **e** Fe-40% As, **f** Fe-45% As, **g** Fe-55% As, **h** Fe-65% As, and **i** Fe-75% As

The phase compositions of the sintered alloys were further confirmed by XRD analyses (Fig. 6a), and the quantitative XRD analysis results are shown in Fig. 6b and Table 2. As shown in Fig. 6a, it is worth noting that the diffraction peak of Fe–As alloys after VHPS was sharper and smoother than that of Fe–As powders after MA, which indicated a good crystallinity of alloys. Similarly, it can be noted that there are also no raw As peaks in the sintered Fe–As alloys, indicating the formation of the solid solution phase or intermetallic phase. The characteristic peaks assigned to  $\alpha$ -Fe and  $\text{Fe}_2\text{As}$  were detected, and the intensity of  $\alpha$ -Fe is significantly higher than that of  $\text{Fe}_2\text{As}$  in the Fe-20% As alloy, suggesting that a lot of As dissolved in  $\alpha$ -Fe to form a solid solution phase ( $\alpha$ -Fe[As]) and little As reacting with Fe to form  $\text{Fe}_2\text{As}$ . Then, the intensity of  $\text{Fe}_2\text{As}$  peaks increased, while the corresponding  $\alpha$ -Fe[As] phases decreased with the increasing weight fraction of As. Furthermore, the solid solution phase  $\alpha$ -Fe[As] and the  $\text{Fe}_2\text{As}$  phases were completely transformed to the FeAs phase in Fe-55% As alloy with the further As addition. The FeAs phases eventually completely transformed to the

$\text{FeAs}_2$  phase in the Fe-75% As alloy with excessive addition of As due to more As being available to react with Fe. XRD results are consistent with the above EDS analysis results.

According to the results (Table 2) obtained from XRD, it can be concluded that the crystallite size of the sintered Fe–As alloys grows significantly with increasing As content; additionally, it is much higher than that of the as-milled Fe–As powders (Table 1) due to relaxation and annihilation of dislocations during VHPS [43]. However, because of the high heating rate, low sintering temperature, and short sintering time of VHPS, the dislocation density and microstrain of the sintered specimens remained much lower than those of the PAMPs. It is worth noting that the average dislocation density of the pre-alloyed Fe-65% As powders (i.e.,  $\sim 9.37$ ) after MA was almost 10 times higher than that of the sintered Fe-65% As alloy (i.e.,  $\sim 0.95$ ) after VHPS. This relatively small microstrain in the sintered Fe-65% As and Fe-75% As is because the powders have undergone certain alloying and intermetallic phases with better crystallinity



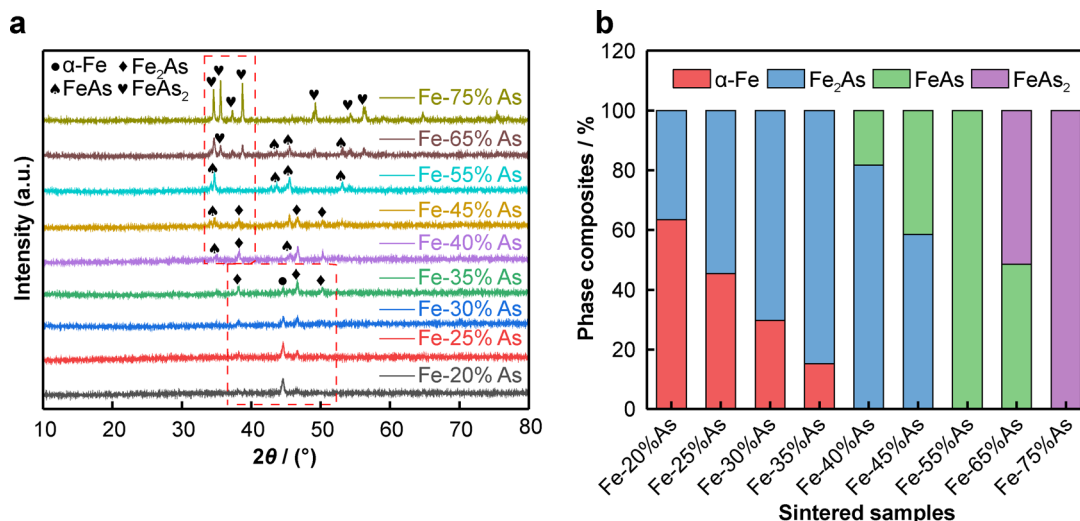


**Fig. 6** **a** XRD patterns of sintered Fe–As alloys and **b** corresponding phase compositions obtained from XRD

**Table 2** Results of XRD analyses of sintered Fe–As alloys by VHPS before and after leaching test by TCLP

Sample	Crystallite size (nm)		Dislocation density ( $10^{15} \text{ m}^{-2}$ )		Strain ( $10^{-3}$ )	
	Before	After	Before	After	Before	After
Fe-20% As	21.99	20.05	2.07	2.73	4.33	4.32
Fe-25% As	22.39	28.78	2.03	2.78	4.25	3.47
Fe-30% As	28.26	29.79	1.41	1.63	3.47	3.21
Fe-35% As	30.28	32.61	1.16	1.05	3.10	3.22
Fe-40% As	30.21	28.78	1.20	1.45	3.14	3.38
Fe-45% As	29.01	30.48	1.46	1.47	3.34	2.98
Fe-55% As	28.44	30.22	1.50	1.14	3.45	3.19
Fe-65% As	34.54	35.81	0.95	0.87	2.77	2.72
Fe-75% As	34.59	42.72	1.44	0.66	2.49	2.10

than other PAMPs formed during the MA process, as shown in Fig. 3.

### 3.2.2 Physical and mechanical properties

The apparent relative density and physical density of sintered Fe–As alloys with different As contents are shown in Fig. 7a. With increasing As content, the relative densities of Fe–As alloys gradually decrease at first and then significantly increase and finally dramatically decrease, reaching a minimum relative density of 88.18% at an As content of 75 wt%. However, the relative densities of sintered Fe–As alloys are all almost higher than 95% except for the Fe-75% As alloy. The Fe-55% As alloy reaches a maximum relative density of 99.20%, which could be attributed to the most uniform phase distributed

without other phases (Figs. 5g, 6b). Similarly, the physical densities are almost higher than  $7.350 \text{ g cm}^{-3}$  except for the Fe-75% As alloy ( $6.702 \text{ g cm}^{-3}$ ). The dramatically decreased density of the Fe-75% As alloy, which was 13.0% lower than that of Fe-20% As, is due to the excessive addition of lightweight As (theoretical density of  $5.727 \text{ g cm}^{-3}$ ) [43].

Figure 7b presents the results of the TCLP and HJ tests for sintered materials. The leaching toxicity of As increases with increasing As content for both the TCLP and HJ methods. However, it should be noted that the leaching concentration of As was less than the United States Environmental Protection Agency (US EPA) limits (As  $5 \text{ mg}\cdot\text{L}^{-1}$ ) when the As content was 20%–30% for both the TCLP and HJ methods. For the TCLP test, the Fe-25% As alloy had the lowest leaching concentration of As ( $2.18 \text{ mg}\cdot\text{L}^{-1}$ ). For the HJ test, there was almost no As leaching when the As content was 20%–30%, and the Fe-30% As alloy had the lowest leaching concentration of As ( $0.06 \text{ mg}\cdot\text{L}^{-1}$ ). According to the toxicity results, 30% of As could be stably solidified in Fe–As alloys, indicating that it is a promising method for As resource utilization. Combining these results with the microstructure (Fig. 4), it could be concluded that a high-density and full-dense microstructural Fe–As alloy with limited toxicity could be obtained by the MA with the subsequent VHPS method.

The effect of As content on the compressive strength and hardness of sintered Fe–As alloys before and after the leaching test is shown in Fig. 7c, d, respectively. As shown in Fig. 7c, the compressive strength of sintered Fe–As alloys by VHPS before and after leaching displayed a downward trend as the As content increased. In addition, it is worth noting that when the As content ranges from 20 to 30%, the compressive strength of these alloys with limited

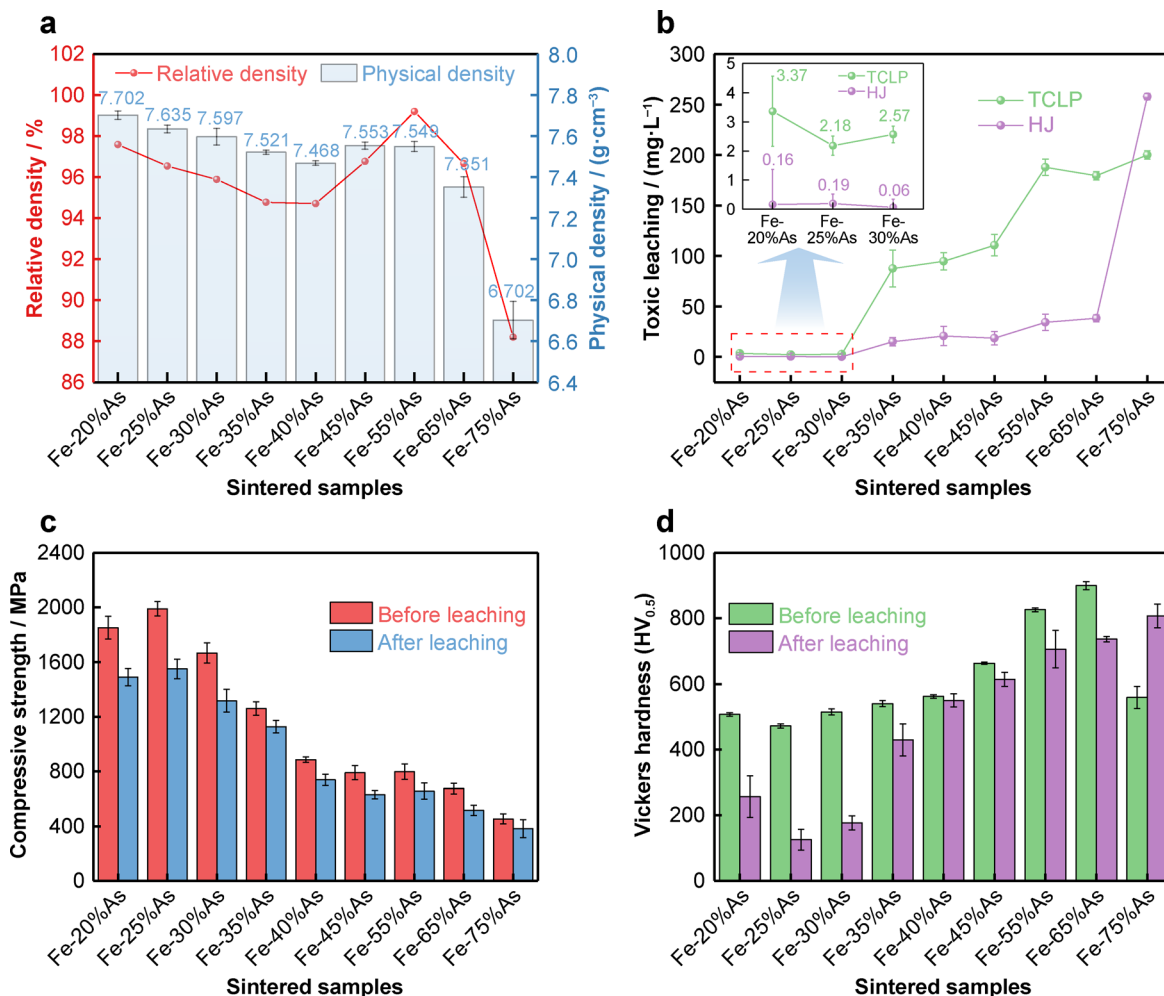


**Fig. 7** **a** Physical density, **b** leaching concentration of As, **c** compressive strength, and **d** Vickers hardness of sintered Fe–As alloys by VHPS with varying As contents before and after leaching test by TCLP

As leaching toxicity exceeds 1500 MPa. In particular, the Fe-25% As alloy before and after leaching has a maximum compressive strength of 1989.19 and 1550 MPa, which are 77.21% and 75.34% higher than that of Fe-75% As, respectively. The higher compressive strength could be attributed to the fine crystallite size, solid solution strengthening, and dislocation strengthening. According to the Hall–Petch equation, the strength and hardness of the alloy decrease as the grain size increases [28]. As shown in Table 2, it is known that the sizes of Fe–As alloys increased, while the dislocation density decreased with the As addition, resulting in a decrease in compressive strength. More importantly, it can be noted that the fraction of the solid solution phase  $\alpha$ -Fe[As] gradually reduced and translated into the intermetallic phase (FeAs) in Fe-40% As alloy (Fig. 6b), resulting in a further dramatic drop in the compressive strength. On the other hand, it can be noted that the Fe-75% As alloy has the largest crystallite size (34.59 nm), the minimum microstrain ( $2.49 \times 10^{-3}$ )

(Table 2), and the aggregation of As particles (Fig. 5i). In addition, The FeAs<sub>2</sub> phase is the only phase in Fe-75% As, so the solid solution strengthening is relatively weak. These factors resulted in the lowest compressive strength (453.38 MPa). Thus, grain refinement, solid solution strengthening, and dislocation strengthening play an important role in compressive strength.

Similarly, after leaching, Fe-20% As, Fe-25% As, and Fe-30% As have higher compressive strength than other Fe–As alloys, with 1490.97, 1550.90, and 1318.11 MPa, respectively. Fe-75% As has the lowest compressive strength (382.46 MPa). Moreover, the compressive strength of these Fe–As alloys after leaching is lower than that of the Fe–As alloys before leaching. This phenomenon may be attributed to the change in the morphology, crystallite size, and phase structure of the sample after leaching. As shown in Figs. S1–S3, the surface of Fe–As alloys with As contents ranging from 20% to 55% was covered by an unconsolidated corrosion layer due to the loss and

oxidation of a large amount of Fe and As elements, which reduced the interfacial bonding of the alloy, and the high concentration of O resulted in weak grain boundary cohesion and reduced the strength of the Fe–As alloys [25, 44], which could be confirmed by the results of mapping (Table S4, Fig. S2). Additionally, according to the Hall–Petch equation, the crystallite size of Fe–As alloys after leaching is higher than that before leaching. Meanwhile, the dislocation density and microstrain of the Fe–As alloys are lower than those of the Fe–As alloys before (Table 2), which would result in a further decrease in compressive strength. On the other hand, the solid solution  $\alpha$ -Fe[As] phase of Fe–As alloys after leaching dramatically decreased compared with that of Fe–As alloys before leaching. These above factors would result in the decrease in Fe–As alloy after leaching.

Figure 7d shows the Vickers hardness of the Fe–As alloys with varying As contents before and after the leaching test. With increasing As content, the hardness of the Fe–As alloys before leaching first increases and subsequently decreases, reaching a maximum of  $HV_{0.5}$  899.41 at an As content of 65%, which is 47.56% higher than that of the Fe-25% As alloy. The following reasons may be responsible for this phenomenon: The Fe and As elements in the PAMPs have undergone certain alloying, the distance between the As and Fe particles decreased, and the bonding increased. Moreover, an intermetallic phase gradually formed as the As content increased from 20 to 65%, which effectively enhanced the hardness of the samples [45, 46]. On the other hand, the distribution of the intermetallic phase gradually became denser and more uniform with As addition, which further strengthened the Vickers hardness by the dispersion effect of the alloys [47]. However, with the excessive increase in As content, the aggregation of As particles became increasingly apparent (Fig. 5i). There is the only  $FeAs_2$  phase for the Fe-75% As alloy without other phases, resulting in the decrease in Vickers hardness ( $HV_{0.5}$  559.39). Therefore, the formation and uniform distribution of the intermetallic phase were effective in improving the Vickers hardness of the Fe–As alloys in this paper. For the effect of grain size, it could be noted that the Vickers hardness results are contrary to the predictions made by the Hall–Petch relationship, which suggests that the grain size is unlikely the dominant factor that affects the hardness of the materials.

After the leaching test, the Vickers hardness of the Fe–As alloys showed a similar trend to that before leaching. Interestingly, it could be noted that the hardness of the Fe-75% As alloy after leaching ( $HV_{0.5}$  806.76) is higher than before ( $HV_{0.5}$  559.39), while other alloys are lower than before, which could be assigned to the denser microstructure. As shown in Fig. S2i, the microstructure of the Fe-75% As alloy after leaching became denser, and the

distribution of elements became more uniform than that before leaching (Fig. 5i). This indicated that the denser microstructure and uniform distribution of elements play an important role in the hardness. However, for other alloys after leaching, the surface of alloys has an unconsolidated corrosion layer due to a large amount of Fe loss and the high concentration of O element, leading to significant decreases in hardness. More elemental separation exists in the sintered Fe–As alloys after leaching, and the intermetallic phase is not uniform (Fig. S2). Additionally, the TCLP leaching eliminates the residual stresses formed during the preparation as well as the processing of the composites, and consequently, the internal hardness is reduced [48]. On the other hand, in comparison with the SEM images of the Fe-65% As before TCLP leaching (Fig. 4h), the number of holes was formed and extended on the surface of Fe-65% As after TCLP leaching, which destroyed the metallurgical bonding interface and decreased the overall mechanical properties of the composite [49]. Combinations of the above factors would lead to a decrease in the hardness after TCLP leaching.

### 3.3 Mechanisms

The detailed mechanism of low As leaching toxicity from Fe–As alloys was explored for As contents ranging from 20%–30%. XPS was used to analyze the changes in the valence states of the Fe-20% As, Fe-65% As, and Fe-75% As alloys after VHPS. The results are presented in Fig. 8 and Table 3. Figure 8a–c displays XPS survey spectra of the three alloys. Fe, As, and O existed in these alloys, and the intensities of Fe 2p and O 1s in the Fe-20% As alloy were greater than those in the other two alloys, which was attributed to the oxidation of Fe and As. In addition, the intensities of As 2p<sub>3/2</sub>, As(A), and As 3d significantly increase with increasing As content, while that of O 1s decreases.

Figure 8d–f shows Fe 2p spectra of the three alloys. As shown in Fig. 8d, combined with XRD and BSE mapping results, the peaks at binding energies (BE) of 706.72 and 717.66 eV for the Fe-20% As alloy could be ascribed to  $\alpha$ -Fe and  $Fe_2As$ , respectively. The prominent peaks at 710.23 eV (2p<sub>3/2</sub>), 713.55 eV (2p<sub>3/2</sub>), 723.30 eV (2p<sub>1/2</sub>), and 726.40 eV (2p<sub>1/2</sub>) corresponding to the binding energy of 2p<sub>3/2</sub> and 2p<sub>1/2</sub> of iron oxide states indicate the existence of oxide in the Fe-20% As alloy, while the satellite peaks were at 719.85 and 730.46 eV [50]. Moreover, the calculated atomic ratio of iron oxide in Fe-20% As is higher than the other two alloys (Table 3), confirming that the content of oxides is higher than that of the other two alloys. Figure 8e displays the Fe 2p spectrum of the Fe-65% As alloy. It could be noted that the BE peaks at 706.83 and 719.67 eV were assigned to the iron–arsenic compounds,

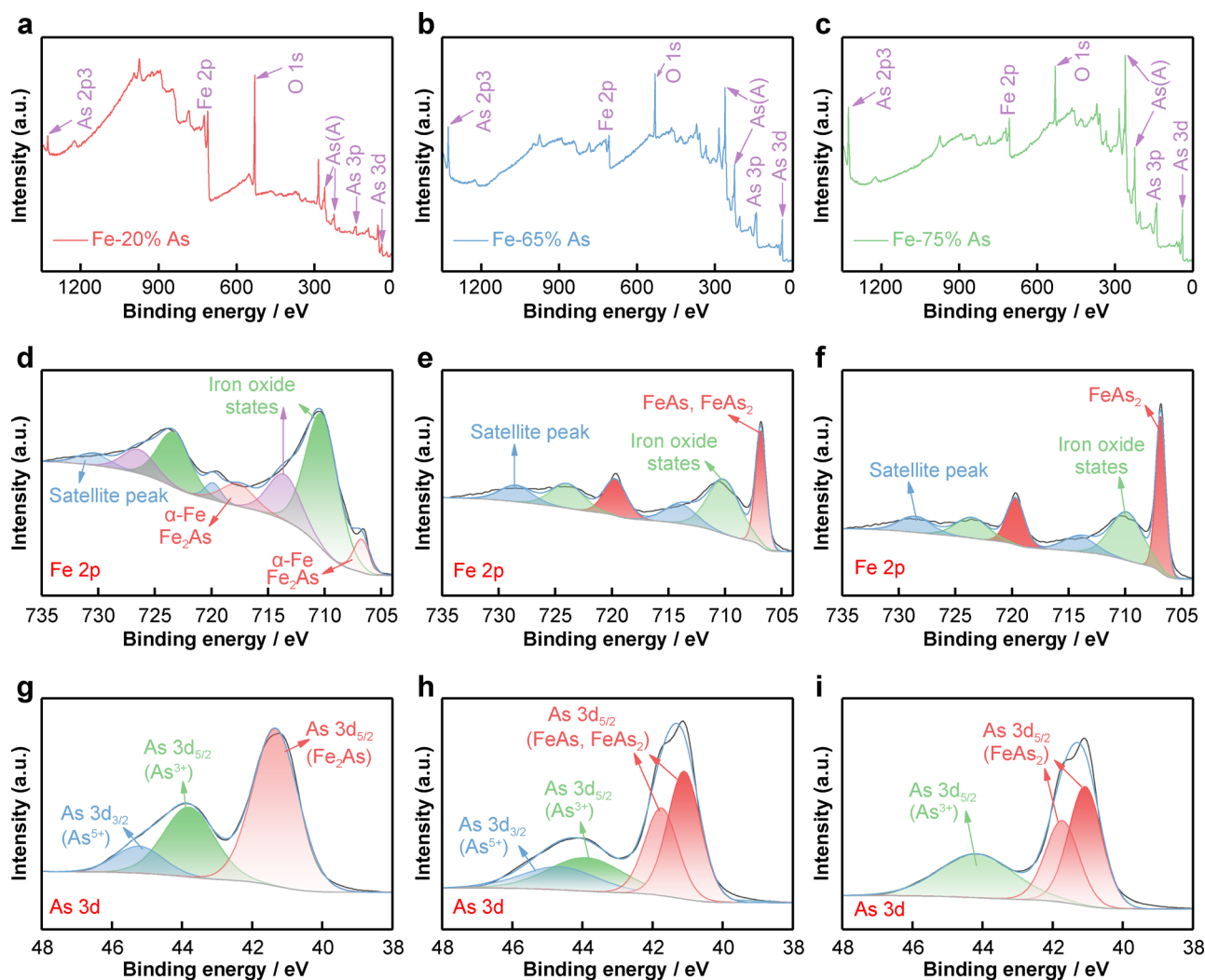


**Fig. 8** a XPS survey spectra, d Fe 2p and g As 3d spectra of Fe-20% As alloy; b XPS survey spectra, e Fe 2p and h As 3d spectra of Fe-65% As alloy; c XPS survey spectra, f Fe 2p and i As 3d spectra of Fe-75% As alloy

while the peaks situated at 710.09 and 723.92 eV were ascribed to the iron oxide states, while the satellite peaks were at 713.94 and 728.49 eV, respectively [51, 52]. The Fe-75% As alloy (Fig. 8f) had similar Fe 2p spectra as the Fe-65% As alloy. According to the calculated atomic ratios in Table 3, it could be known that the content of iron oxide dramatically decreased with As addition, while that of the iron–arsenic compounds significantly increased.

Additionally, the As 3d spectra of the three alloys were also analyzed (Fig. 8g–i). As shown in Fig. 8g, there are three peaks at 41.33, 43.80, and 45.22 eV in the Fe-20% As alloy, which could be ascribed to the iron–arsenic compounds ( $\text{Fe}_2\text{As}$ ),  $\text{As}^{3+}$  and  $\text{As}^{5+}$  oxide, respectively [51, 53]. According to the fitted results, compared with the As 3d spectra of Fe-20% As alloy, the  $\text{As}^{3+}$  and  $\text{As}^{5+}$  oxide contents of Fe-65% As alloy decreased (Fig. 8h), while that of Fe-75% As alloy further increased and completely translated into  $\text{As}^{3+}$  oxide due to the excessive

As addition (Fig. 8i). In brief, the iron oxides play an important role in the leaching process, resulting in the low toxicity of the Fe-20% As alloy.

To further clarify the strengthening mechanisms of the alloys, Fe-20% As and Fe-75% As were analyzed via EBSD. Figure 9 shows the inverse pole figures (IPF) of ND orientation (IPF-Z), grain boundaries (GBs), phase maps, and the grain size distributions of the Fe-20% As and Fe-75% As alloys. As shown in Fig. 9b, f, although axial pressure was applied during the VHPS process, the two Fe–As alloys had no obvious grain orientation preference. There are many fine grains in the Fe-20% As alloy, and the average grain size is 0.39  $\mu\text{m}$  (Fig. 9e); however, as the fraction of coarse grains increases, the distribution of grains becomes relatively uniform with the As addition in the Fe-75% As alloy due to the increase in grain size. The average grain size of Fe-75% As alloy is 0.56  $\mu\text{m}$  (Fig. 9i). This trend agrees with the XRD calculated results. The



**Table 3** XPS spectra fitting results for Fe-20% As, Fe-65% As, and Fe-75% As alloys

Samples	Peak	BE (eV)	Content (wt%)	FWHM (a.u.)		
Fe-20% As alloy	Fe	706.72	5.11	1.67		
		2p	710.23	42.05	3.36	
			713.55	14.43	3.36	
			717.66	7.07	3.36	
			719.85	2.68	1.67	
			723.30	17.39	3.36	
			726.40	7.56	3.36	
			730.46	3.70	3.36	
	As		41.33	59.40	1.52	
		3d	43.80	29.81	1.71	
			45.22	10.79	1.60	
	Fe-65% As alloy	Fe	706.83	21.35	1.12	
			2p	710.09	30.21	3.36
			713.94	10.77	3.36	
			719.67	14.47	2.36	
			723.92	13.96	3.36	
			728.49	9.25	3.36	
As				41.11	38.18	1.13
		3d	41.77	26.20	1.13	
			43.72	20.17	1.88	
			45.03	15.46	1.99	
		Fe-75% As alloy	Fe	706.86	27.09	1.03
				2p	709.83	27.60
				714.04	8.89	3.36
	719.67			14.99	1.88	
	723.53			12.02	3.36	
	728.56			9.41	3.36	
As				41.08	39.74	1.12
	3d		41.73	27.28	1.12	
		44.17	32.98	2.51		

GBs map of the two alloys is displayed in Fig. 9c and g. The black lines were represented as high-angle grain boundaries (HAGBs,  $> 15$  misorientation), while the red lines represented low-angle grain boundaries (LAGBs,  $> 2$  misorientation). The majority of grains were filled with HAGBs (96.40%) in the Fe-20% As sample, and the fraction of HAGBs of the Fe-75% As alloy increased (97.70%). Moreover, the fraction of LAGBs decreased from 3.60 to 2.30%, implying that recrystallization of the microstructure occurred and the microstructure softening occurred [54]. LAGBs prefer to be located around ultra-

fine grains as well as in the grain interior of elongated grains. In contrast, coarse recrystallized grains are always dislocation-free because grain growth has consumed the stored strain energy. This suggested that the density of dislocations decreased in the Fe-75% As alloy, resulting in the reduction of compressive strength. Figure 9d, h shows the phase fraction of two alloys, respectively. The Fe-20% As produced the majority of the  $\alpha$ -Fe phase (73.80%) and a small portion of  $\text{Fe}_2\text{As}$  phase (11.70%) as well as zero solution. However, the Fe-75% As sample exhibited a relatively uniform single-phase ( $\text{FeAs}_2$  phase, 84.76%) and minor zero solution (15.24%).

On the other hand, the pole figures and inverse pole figures maps of the  $\alpha$ -Fe and  $\text{Fe}_2\text{As}$  of the Fe-20% As and Fe-75% As alloy are shown in Fig. 10 and S4, respectively. These results confirmed that the  $\alpha$ -Fe of the Fe-20% As alloy had relatively uniform hot spots on the {100}, {110}, and {111} planes (Fig. 10a), indicating that a large amount of the solid solution phase was dispersed in this alloy. Moreover, the  $\alpha$ -Fe phase had obvious crystallographic orientation along with (001) direction (Fig. S4a). The  $\text{Fe}_2\text{As}$  phase had hot spots focused on the {010} and {001} planes, and the maximum value of pole intensity was 4.60 (Fig. 10b). However, as shown in Fig. 10c and S4c, a weaker basal fiber texture with an intensity of 2.50 can be observed in the Fe-75% As alloy, although the crystallographic orientation was along (001) direction. The stronger basal texture directly hindered the migration of dislocation, resulting in a higher compressive strength in the Fe-20% As alloy.

For a more detailed examination of the morphology and dislocation distribution of the two alloys, the samples were characterized by the combination of FIB and TEM. Figure 11 shows TEM bright field (BF) images of the Fe-20% As and the Fe-75% As alloys. As shown in Fig. 11a, d, the Fe-20% As consists of the most fine grains, while the Fe-75% As is filled with coarse grains, which is consistent with the grain size distribution of results obtained from EBSD. Moreover, as shown in the BF images of the Fe-20% As, there are a large number of dislocations, as marked by the white arrow, distributed to the surface of coarse grains. However, the density of dislocation distribution decreased as displayed in the BF images of the Fe-75% As, which may be ascribed to the excess As added resulting in the porosity level increase.

According to the above discussion and results, iron oxides play an important role in the low toxicity of Fe-As alloys. Grain size strengthening, solid solution strengthening, and dislocation strengthening mechanisms play vital roles in enhancing the compressive strength of Fe-As alloys.

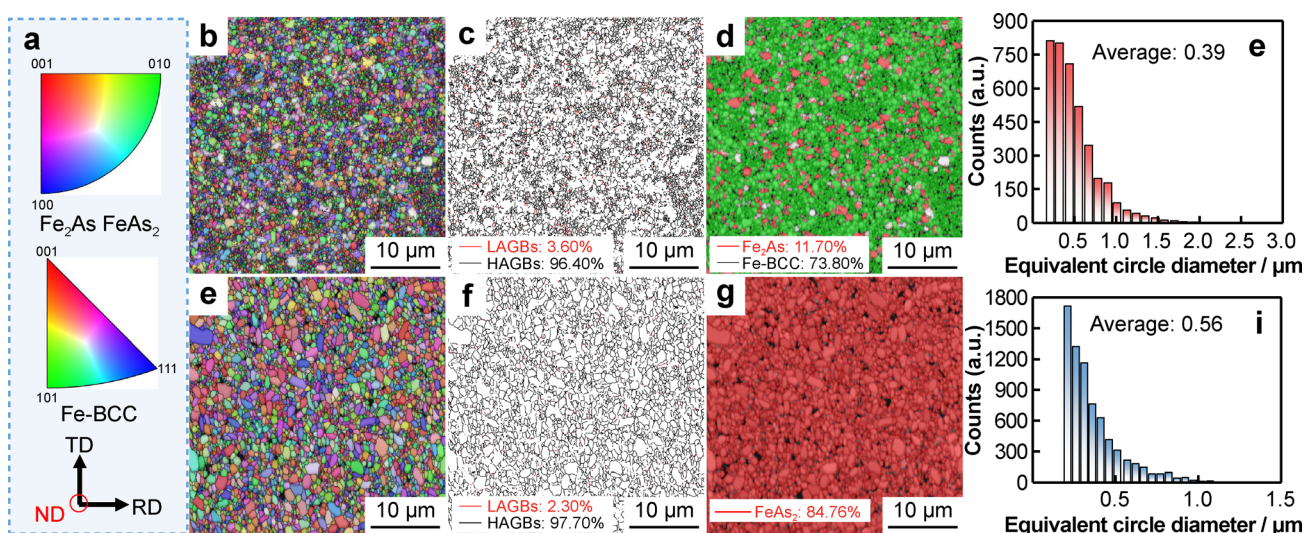


**Fig. 9** **a** Legend for IPF maps; **b, f** IPF of ND orientation (IPF-Z); **c, g** phase maps; **d, h** GBs maps; **e, i** grain size distributions of Fe-20% As alloy and Fe-75% As alloy

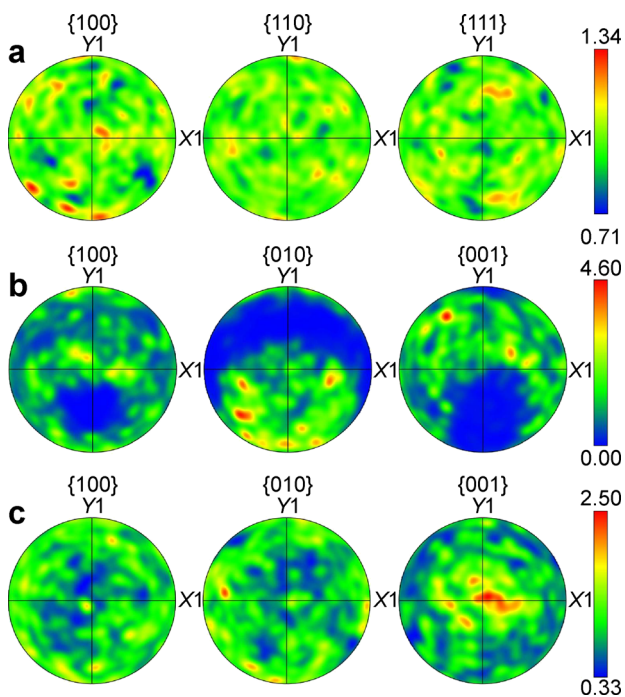


**Fig. 10** EBSD-derived pole figures of **a**  $\alpha$ -Fe, **b**  $\text{Fe}_2\text{As}$  of Fe-20% As, and **c** Fe-75% As alloys

The intermetallic phase strengthening mechanism and dispersion effect contributed significantly to the Vickers hardness of the Fe–As alloys compared to those of the grain size strengthening and solid solution strengthening.

#### 4 Conclusion

In this work, novel high-performance Fe–As alloys with limited toxicity were prepared by MA, followed by VHPS. The effects of As addition on the microstructure, phase composition, physical properties, leaching toxicity, mechanical performance, and corresponding mechanism of sintered Fe–As alloys by VHPS before and after leaching by TCLP were systematically studied. With the content of As increasing, a nearly fully densified Fe–As alloy was obtained, and the Vickers hardness of sintered Fe–As alloys was improved, while the physical density and compressive strength decreased. The physical densities of sintered alloys are almost higher than  $7.350 \text{ g}\cdot\text{cm}^{-3}$  except for the Fe-75% As alloy ( $6.702 \text{ g}\cdot\text{cm}^{-3}$ ) due to the excessive As addition. The leaching concentration of As was less than the EPA limits ( $\text{As } 5 \text{ mg}\cdot\text{L}^{-1}$ ) when the As content was 20%–30% for both the TCLP and HJ methods. The Fe-25% As alloy before and after leaching reaches 1989.19 and 1550.9 MPa, which are 77.21% and 75.34% higher than that of Fe-75% As, respectively. The Fe-65% As alloy had the maximum hardness ( $\text{HV}_{0.05} 899.41$ ). The relatively reasonable compressive strength could be attributed to the grain size strengthening, solid solution strengthening, and dislocation strengthening mechanisms, while the intermetallic phase strengthening mechanisms and the dispersion effect contributed significantly to the Vickers hardness. The excellent mechanical properties



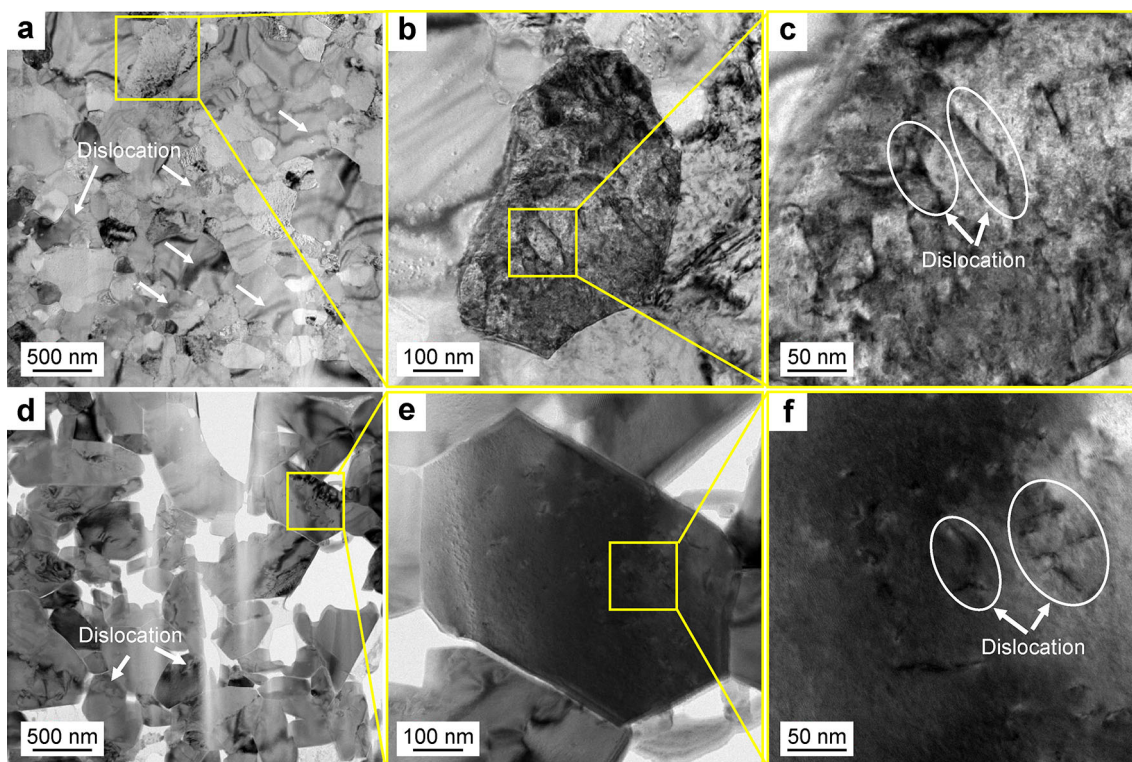


**Fig. 11** TEM bright field (BF) images of **a, b, c** Fe-20% As and **d, e, f** Fe-75% As alloys

enable Fe–As alloys to have potential applications in the high-value utilization of As resources.

**Acknowledgments** This work was financially supported by the National Natural Science Foundation of China (No. 52104406), the Natural Science Foundation of Hunan Province (No. 2022JJ20074), the Foundation for Innovative Research Groups of the National Natural Science Foundation of China (No. 52121004) and the National Natural Science Foundation of China for Distinguished Young Scholars (No. 51825403).

#### Declarations

**Conflict of interests** The authors declare that they have no conflict of interest.

#### References

- [1] Zhang XW, Zhang KJ, Shi Y, Xiang HR, Yang WC, Zhao FP. Surface engineering of multifunctional nanostructured adsorbents for enhanced wastewater treatment: a review. *Sci Total Environ.* 2024;920: 170951. <https://doi.org/10.1016/j.scitotenv.2024.170951>.
- [2] He LH, Huang R, Luo JX, Lv XD, Mao JC, Zhang JZ. Study on the interaction mechanism in the Pr–Fe–As system. *Mater Res Express.* 2020;7(11): 116507. <https://doi.org/10.1088/2053-1591/abc58d>.
- [3] Wang YG, Han FL, Mu JQ. Solidification/stabilization mechanism of Pb(II), Cd(II), Mn(II) and Cr(III) in fly ash based geopolymers. *Constr Build Mater.* 2018;160:818. <https://doi.org/10.1016/j.conbuildmat.2017.12.006>.
- [4] Xia M, Muhammad F, Zeng LH, Li S, Huang X, Jiao BQ, Shiau YC, Li DW. Solidification/stabilization of lead-zinc smelting slag in composite based geopolymer. *J Cleaner Prod.* 2019;209: 1206. <https://doi.org/10.1016/j.jclepro.2018.10.265>.
- [5] Zhang YY, Zhang SQ, Ni W, Yan QH, Gao W, Li YY. Immobilization of high-arsenic-containing tailings by using metallurgical slag-cementing materials. *Chemosphere.* 2019; 223:117. <https://doi.org/10.1016/j.chemosphere.2019.02.030>.
- [6] Li JS, Chen L, Zhan BJ, Wang L, Poon CS, Tsang DCW. Sustainable stabilization/solidification of arsenic-containing soil by blast slag and cement blends. *Chemosphere.* 2021;271: 129868. <https://doi.org/10.1016/j.chemosphere.2021.129868>.
- [7] Xia WY, Du YJ, Li FS, Li CP, Yan XL, Arulrajah A, Wang F, Song DJ. In-situ solidification/stabilization of heavy metals contaminated site soil using a dry jet mixing method and new hydroxyapatite based binder. *J Hazard Mater.* 2019;369:353. <https://doi.org/10.1016/j.jhazmat.2019.02.031>.
- [8] Sun X, Guo Y, Wu G, Zhao Y, Li H. Research of n-type arsenic doped diamond: Theoretical analysis of electronic and mechanical properties. *Diamond Relat Mater.* 2020;108: 107924. <https://doi.org/10.1016/j.diamond.2020.107924>.
- [9] Mauersberger T, Ibrahim I, Grube M, Heinzig A, Weber WM. Size effect of electronic properties in highly arsenic-doped silicon nanowires. *Solid-State Electron.* 2019;168: 107724. <https://doi.org/10.1016/j.sse.2019.107724>.
- [10] Tian F, Ren Z. High thermal conductivity in boron arsenide: from prediction to reality. *Angew Chem Int Ed Engl.* 2019; 58(18):5824. <https://doi.org/10.1002/anie.201812112>.
- [11] Dames C. Ultrahigh thermal conductivity confirmed in boron arsenide. *Science.* 2018;361(6402):549. <https://doi.org/10.1126/science.aau4793>.
- [12] Tian F, Song B, Chen X, Ravichandran NK, Lv YC, Chen K, Sullivan S, Kim J, Zhou YY, Liu TH, Goni M, Ding ZW, Sun JJ, Gamage G, Sun HR, Ziyace H, Huyan SY, Deng LZ, Zhou JS, Schmidt AJ, Chen S, Chu CW, Huang PY, Broido D, Shi L, Chen G, Ren ZF. Unusual high thermal conductivity in boron

- arsenide bulk crystals. *Science*. 2018;361(6402):582. <https://doi.org/10.1126/science.aat793>.
- [13] Zhou Y, Wang YY, Liang YJ, Zhou YW, Liu ZX, Peng C, Ke Y, Min XB. Microstructure and magnetic properties of FeAs with coarse-grain and nanocrystalline structure. *Trans Nonferrous Met Soc China*. 2022;32(3):972. [https://doi.org/10.1016/s1003-6326\(22\)65847-3](https://doi.org/10.1016/s1003-6326(22)65847-3).
- [14] Ziq K, Salem A. Magnetic properties of FeAs single crystal. *J Supercond Novel Magn*. 2013;26:1185. <https://doi.org/10.1007/s10948-012-2013-3>.
- [15] Jiao Y, Wu W, Ma F, Yu ZM, Lu Y, Sheng XL, Zhang Y, Yang SA. Room temperature ferromagnetism and antiferromagnetism in two-dimensional iron arsenides. *Nanoscale*. 2019;11(35):16508. <https://doi.org/10.1039/C9NR04338A>.
- [16] Song JQ, Chai LY, Liang YJ, Wang HY, Lin Z, Liu ZX, Liao Y, Lai XT, Peng C. From highly oriented bulk black arsenic phosphorus to well-crystallized exfoliated flakes with enhanced anti-oxidation: precise control upon chemical vapor transport. *J Mater Chem C*. 2023;11(14):4683. <https://doi.org/10.1039/d3tc00338h>.
- [17] Zhao FP, Wang DY, Zhang F, Cui BC, Xia QL, Zhong MZ. Gate-controlled photoresponse improvement in b-AsP/WSe<sub>2</sub> heterostructures with type-I band alignment. *Appl Phys Lett*. 2023;122: 151105. <https://doi.org/10.1063/5.0144982>.
- [18] The NP, Toan HN, Thao DN, Hieu HK. Temperature and size effects on the oscillatory frequency of electron velocity in p-i-n GaAs semiconductor. *Phys Lett A*. 2022;445: 128240. <https://doi.org/10.1016/j.physleta.2022.128240>.
- [19] Alhaj Ali A, Shaer A, Elsaid M. Simultaneous effects of Rashba, magnetic field and impurity on the magnetization and magnetic susceptibility of a GaAs-semiconductor quantum ring. *J Magn Magn Mater*. 2022;556: 169435. <https://doi.org/10.1016/j.jmmm.2022.169435>.
- [20] Masi A, Angrisani Armenio A, Augieri A, Celentano G, Duchenko A, Rufoloni A, Vannozzi A, Varsano F, Della CA. Cu/Ta sheaths for iron-based superconductors: First experimental findings in Ca/K-1144 wires. *Superconductivity*. 2022;2: 100014. <https://doi.org/10.1016/j.supcon.2022.100014>.
- [21] Cheng Z, Dong CH, Yang H, Zhang QH, Awaji S, Gu L, Wen HH, Ma Y. Strengthened proximity effect at grain boundaries to enhance inter-grain supercurrent in Ba1-KFe<sub>2</sub>As<sub>2</sub> superconductors. *Mater Today Phys*. 2022;28: 100848. <https://doi.org/10.1016/j.mtphys.2022.100848>.
- [22] Muthaiah R, Garg J. Strain tuned thermal conductivity reduction in Indium Arsenide (InAs) – A first-principles study. *Comput Mater Sci*. 2021;196: 110531. <https://doi.org/10.1016/j.commatsci.2021.110531>.
- [23] Rezeq MD, Abbas Y, Wen B, Wasilewski Z, Ban D. Direct detection of electronic states for individual indium arsenide (InAs) quantum dots grown by molecular beam epitaxy. *Appl Surf Sci*. 2022;590: 153046. <https://doi.org/10.1016/j.apsusc.2022.153046>.
- [24] Xin WB, Song B, Huang CG, Song MM, Song GY. Effect of arsenic content and quenching temperature on solidification microstructure and arsenic distribution in iron-arsenic alloys. *Int J Miner Metall Mater*. 2015;22(7):704. <https://doi.org/10.1007/s12613-015-1125-8>.
- [25] Shi RZ, Shi HJ, Liang JF, Tong ZB, Zhou Y, Wang Q. Effects of the cooling rate on the solidified structure and toxic leaching of an arsenic matte. *Waste Biomass Valorization*. 2021;12(9):5249. <https://doi.org/10.1007/s12649-021-01388-z>.
- [26] Wu L, Yu ZJ, Liu C, Ma Y, Huang Y, Wang T, Yang L, Yan H, Liu W. Microstructure and tensile properties of aluminum powder metallurgy alloy prepared by a novel low-pressure sintering. *J Mater Res Technol*. 2021;14:1419. <https://doi.org/10.1016/j.jmrt.2021.07.074>.
- [27] Duan YT, Liu WS, Ma YZ, Cai QS, Zhu WT, Li J. Effect of Ni addition upon microstructure and mechanical properties of hot isostatic pressed 30CrMnSiNi2A ultrahigh strength steel. *Mater Sci Eng: A*. 2022;850: 143599. <https://doi.org/10.1016/j.msea.2022.143599>.
- [28] Liu XQ, Cheng H, Li ZJ, Wang H, Chang F, Wang W, Tang Q, Dai P. Microstructure and mechanical properties of FeCoCr-NiMnTi<sub>0.1</sub>C<sub>0.1</sub> high-entropy alloy produced by mechanical alloying and vacuum hot pressing sintering. *Vacuum*. 2019;165: 297. <https://doi.org/10.1016/j.vacuum.2019.04.043>.
- [29] Zhang WJ, Yi H, Cao HJ, Huang JK. Laser additive manufacturing of refractory high entropy alloys: research progress and prospects. *Chin J Rare Met*. 2023;47(5):601. <https://doi.org/10.13373/j.cnki.cjrm.XY22100003>.
- [30] You JS, Hong SH. Densification mechanism and microstructure development of Fe-Ni alloys consolidated by field assisted sintering. *J Alloys Compds*. 2021;884: 161102. <https://doi.org/10.1016/j.jallcom.2021.161102>.
- [31] Deirmina F, Pellizzari M. Strengthening mechanisms in an ultrafine grained powder metallurgical hot work tool steel produced by high energy mechanical milling and spark plasma sintering. *Mater Sci Eng A*. 2019;743:349. <https://doi.org/10.1016/j.msea.2018.11.093>.
- [32] Song XY, Li Y, Zhang F. Microstructural evolution and mechanical properties of Ni-45Ti-5Al-2Nb-1Mo alloy subjected to different heat treatments. *Rare Met*. 2023;42(8):2774. <https://doi.org/10.1007/s12598-019-01318-y>.
- [33] Li SC, Wang QL, Yao Y, Sang DD, Zhang HW, Zhang GZ, Wang C, Liu CL. Application of high-pressure technology in exploring mechanical properties of high-entropy alloys. *Tungsten*. 2023;5(1):50–60. <https://doi.org/10.1007/s42864-021-00132-3>.
- [34] Fan HJ, Liu Y, Ye JW, Qiu WB, Qiu YC. Microstructure and mechanical properties of WC-(Ti, M)(C, N)-Co cemented carbides with different nitrogen contents. *Rare Met*. 2022;41(10): 3530. <https://doi.org/10.1007/s12598-016-0737-0e>.
- [35] Seyyedini S, Zangi H, Bozorgmehr M, Ghasemi B, Tavallaie MM, Adib S. The effect of mechanical alloying time on the microstructural and mechanical properties of spark plasma sintered Ta–10W. *Mater Sci Eng A*. 2020;798:140024. <https://doi.org/10.1016/j.msea.2020.140024>.
- [36] Li D, Hui SX, Ye WJ, Li CL. Microstructure and mechanical properties of a new high-strength and high-toughness titanium alloy. *Rare Met*. 2023;42(1):281. <https://doi.org/10.1007/s12598-016-0722-7>.
- [37] Meher BS, Samantaray PR, Saha R, Chaira D. Effect of dry milling and MWCNTs content during fabrication of Fe-MWCNTs metal matrix composite by high energy planetary milling followed by conventional sintering. *Adv Powder Technol*. 2022;33(2): 103447. <https://doi.org/10.1016/j.apt.2022.103447>.
- [38] Koch CC. Structural nanocrystalline materials: an overview. *J Mater Sci*. 2007;42:1430. <https://doi.org/10.1007/s10853-006-0609-3>.
- [39] Williamson GK, Hall W. X-ray line broadening from filed aluminum and wolfram. *Acta Metall*. 1953;1(1):22. [https://doi.org/10.1016/0001-6160\(53\)90006-6](https://doi.org/10.1016/0001-6160(53)90006-6).
- [40] Ibrahim GS, Kamil KK, Lawan ST, Aminu M, Idris MC, Suleiman BA, Sani GDI. X-ray diffraction (XRD) profile analysis and optical properties of Klockmannite copper selenide nanoparticles synthesized via microwave assisted technique. *Ceram Int*. 2023;49(8):12309. <https://doi.org/10.1016/j.ceramint.2022.12.086>.
- [41] Fadonougbo J, Jung J, Suh J, Lee Y, Shim JH, Fleury E, Young WC. The role of Fe particle size and oxide distribution on the hydrogenation properties of ball-milled nano-crystalline powder mixtures of Fe and Mg. *J Alloys Compds*. 2019;806:1039. <https://doi.org/10.1016/j.jallcom.2019.07.318>.





- [42] Shu YX, Cao HZ, Zhang HB, Xu SH, Hou GY, Tang YP, Zheng GQ. Composition and structure of arsenic–antimony alloy electrodeposited from acidic chloride solution. *Trans Nonferrous Met Soc China*. 2021;31(9):2861. [https://doi.org/10.1016/S1003-6326\(21\)65699-6](https://doi.org/10.1016/S1003-6326(21)65699-6).
- [43] Antonatos N, Mazanek V, Plutnarová I, Sofer Z. Mineralizer-free synthesis of orthorhombic arsenic-phosphorus alloys. *FlatChem*. 2021;30:100297. <https://doi.org/10.1016/j.flatc.2021.100297>.
- [44] Chen X, Lin B, Wang T, Li R, Wang J, Ren S, Zhang GJ. Strengthening mechanisms of Mo-La<sub>2</sub>O<sub>3</sub> alloys processed by solid-solid doping and vacuum hot-pressing sintering. *Vacuum*. 2018;152:70. <https://doi.org/10.1016/j.vacuum.2018.03.012>.
- [45] Mojtahedi M, Aboutalebi MR, Ghaffari M, Soleimani V. Investigation on the formation of Cu–Fe nanocrystalline super-saturated solid solution developed by mechanical alloying. *J Alloys Compds*. 2013;550:380. <https://doi.org/10.1016/j.jallcom.2012.10.112>.
- [46] Hou M, Gao JY, Yang L, Ullah E, Hu T, Guo SH, Hu LT, Li YX. The role of pre-alloyed powder combined with pressure-less microwave sintering on performance of superhard materials. *J Alloys Compds*. 2013;831: 154744. <https://doi.org/10.1016/j.jallcom.2020.154744>.
- [47] Bao R, Yi JH. Densification and alloying of microwave sintering WC–8wt%Co composites. *Int J Refract Met Hard Mater*. 2014; 43:269. <https://doi.org/10.1016/j.ijrmhm.2013.12.010>.
- [48] Fernandez R, Cabeza S, Mishurova T, Fernandez-Castrillo P, Gonzalez-Doncel G, Bruno G. Residual stress and yield strength evolution with annealing treatments in an age-hardenable aluminum alloy matrix composite. *Mater Sci Eng A*. 2018;731:344. <https://doi.org/10.1016/j.msea.2018.06.031>.
- [49] Sequeira CAC, Amaral L. Role of Kirkendall effect in diffusion processes in solids. *Trans Nonferrous Met Soc China*. 2014; 24(1):1. [https://doi.org/10.1016/S1003-6326\(14\)63021-1](https://doi.org/10.1016/S1003-6326(14)63021-1).
- [50] Wang WH, Hu BB, Wang CL, Cui ZJ, Zhao ZW, Yang C. Cr (VI) removal by micron-scale iron-carbon composite induced by ball milling: The role of activated carbon. *Chem Eng J*. 2020; 389: 122633. <https://doi.org/10.1016/j.cej.2019.122633>.
- [51] Jones RA, Wayne NH. XPS evidence for Fe and As oxidation states and electronic states in loellingite (FeAs<sub>2</sub>). *Am Mineral*. 2002; 87(11–12):1692. <https://doi.org/10.2138/am-2002-11-1219>.
- [52] Chai F, Zhang R, Min XB, Yang ZH, Chai LY, Zhao FP. Highly efficient removal of arsenic (III/V) from groundwater using nZVI functionalized cellulose nanocrystals fabricated via a bioinspired strategy. *Sci Total Environ*. 2022;842: 156937. <https://doi.org/10.1016/j.scitotenv.2022.156937>.
- [53] Zhang XM, Wang C, Qian XF, Xie Y, Qian YT. Synthesis of nanocrystalline iron monoarsenide via a reductive recombination pathway. *J Solid State Chem*. 1999;144(2):237. <https://doi.org/10.1006/jssc.1998.8103>.
- [54] Liu ZY, Gao QZ, Zhang HL, Luo SH, Zhang X, Li W, Jiang Y, Li HJ. EBSD analysis and mechanical properties of alumina-forming austenitic steel during hot deformation and annealing. *Mater Sci Eng A*. 2019;755:106. <https://doi.org/10.1016/j.msea.2019.04.005>.

Springer Nature or its licensor (e.g. a society or other partner) holds exclusive rights to this article under a publishing agreement with the author(s) or other rightsholder(s); author self-archiving of the accepted manuscript version of this article is solely governed by the terms of such publishing agreement and applicable law.